

# Aeroelastic stability analysis of an aircraft design: ensuring flutter-free operation

Corentin Latimier<sup>b</sup>, Manuel Sandoval<sup>b</sup>

<sup>a</sup>*Polytechnique Montréal, Department of Aerospace Engineering, 2500 Chem. de Polytechnique, Montréal, QC H3T 1J4, Québec, Canada*

<sup>b</sup>*Concordia University, Department of Aerospace Engineering, 1455 De Maisonneuve Blvd. W., Montréal, QC H3G 1M8, Québec, Canada*

---

## Abstract

This paper presents an aeroelastic analysis of an aircraft design, addressing critical deficiencies in divergence and flutter speeds that rendered the initial configuration non-compliant with regulatory standards. To achieve compliance, a modification to the rear wing structure was proposed, incorporating high-performance materials to shift the center of mass forward, resulting in a design that satisfies safety margins for aeroelastic stability. The analysis extends to evaluate an all-electric variant of the aircraft, examining the impact of mass redistribution due to battery storage on aeroelastic behavior and identifying operational constraints and design adaptations necessary for regulatory compliance. Additionally, a novel methodological contribution is introduced through the application of a modal shape-based approach within the p-k method framework, providing consistent results with traditional techniques while laying the groundwork for further refinement. These findings highlight the importance of iterative design, advanced analytical methods, and a holistic approach to achieving safety, performance, and sustainability in modern aircraft development.

**Keywords:** Aeroelasticity, Flutter, Divergence, p-k method

---

## 1. Introduction

Flutter is a dynamic aeroelastic instability caused by the interaction of aerodynamic, elastic, and inertial forces, posing a critical challenge in aircraft design due to its potential to cause uncontrollable vibrations and structural failure. Ensuring flutter-free operation during the pre-design phase is crucial for safety and performance. Numerical simulations are essential for predicting aeroelastic stability by analyzing the interplay of structural and aerodynamic forces across the flight envelope, ensuring safe operation within the intended environment.

This study examines the aeroelastic stability of a general aviation aircraft being developed by a Canadian company for use in Canada and the United States. Analytical modeling and eigenvalue analysis are employed to demonstrate the aircraft's flutter and divergence-free design, ensuring compliance with FAR 23.2005 (1) regulations. These regulations require configurations to be free from flutter, control reversal, and divergence across and beyond the flight envelope, with a recommended flutter margin of 15% (2).

To evaluate compliance in the preliminary design phase, this paper focuses on divergence and flutter, excluding control reversal as it depends on control surfaces addressed later in the design process. Since divergence occurs typically for higher dynamic pressure than flutter, it requires only a quick verification and therefore, the primary focus of this paper is identifying flutter onset under different operating conditions to guide design modifications and assess environmental, economic, and regulatory impacts.

The theoretical framework introduces models for divergence and flutter. Flutter results are validated against literature benchmarks to ensure reliability. Aeroelastic analysis is conducted

across the entire flight envelope, with design modifications proposed if regulations are not met.

The analysis considers two configurations: one with an internal combustion engine and the other with electric propulsion. Results highlight the static and dynamic behavior for each case, informing potential design or operational changes and their environmental and economic implications.

## 2. Theoretical background

In most modern aircraft, flutter is the primary aeroelastic instability to manifest, as it generally occurs at a lower dynamic pressure than divergence. Consequently, flutter often becomes the primary focus in aeroelastic analyses. However, assessing divergence remains important, as it provides valuable insights into the structural stiffness of the aircraft. While divergence typically occurs at higher dynamic pressures beyond the flutter boundary, analyzing it ensures a comprehensive evaluation of the design and compliance with regulatory standards. This dual analysis strengthens confidence in the safety and robustness of the structure, even under extreme conditions.

### 2.1. Divergence analysis of a uniform flexible wing

The wing of an aircraft may be modeled as a flexible beam clamped on the fuselage and free at the wing tip. The governing equation for the static behavior of a clamped-free wing subjected to torsion can be written as:

$$\frac{d^2\theta}{dy^2} + \lambda^2\theta = -\lambda^2(\alpha_r + \bar{\alpha}_r) \quad (1)$$

where  $\lambda^2 = \frac{q c c_{l_\alpha} \tilde{e}}{\overline{GJ}}$ , with  $\overline{GJ}$  representing the torsional stiffness of the wing's cross-section,  $q$  the dynamic pressure,  $\tilde{e}$  the distance between the elastic axis and the aerodynamic center,  $c$  the chord length, and  $c_{l_\alpha}$  the lift-curve slope. The general solution of equation 2.1 is given by :

$$\theta(y) = A \sin \lambda y + B \cos \lambda y - (\alpha_r + \bar{\alpha}_r)$$

The boundary conditions for a clamped-free flexible wing represent the zero twist and zero twisting moment behavior respectively, being defined by:

$$\theta(0) = 0 \quad \text{and} \quad \frac{\partial \theta}{\partial y} \Big|_{y=l} = 0$$

Incorporating these boundary conditions in the general solution gives:

$$\theta(y) = (\alpha_r + \bar{\alpha}_r) [\tan(\lambda l) \sin(\lambda y) + \cos(\lambda y) - 1] \quad (2)$$

It is observed that the divergence condition occurs when  $(\lambda l)$  reaches  $\pi/2$ , at which point the tangent becomes undefined. Therefore, the divergence dynamic pressure can be determined by using the definition of  $\lambda$ , as follows:

$$q_D = \left( \frac{\pi}{2l} \right)^2 \frac{\overline{GJ}}{c c_{l_\alpha} \tilde{e}} \quad (3)$$

This expression, which accounts for torsional rigidity ( $\overline{GJ}$ ), wing span ( $l$ ), chord length ( $c$ ), lift-curve slope ( $c_{l_\alpha}$ ), and the distance between the aerodynamic center and the elastic axis ( $\tilde{e}$ ), offers a static solution for predicting divergence speeds. These speeds depend on dynamic pressure ( $q$ ), which varies with air density and consequently changes with altitude.

Regarding the lift-curve slope, various models estimate this parameter based on wing characteristics. Three-dimensional effects significantly reduce the value compared to the 2D case. Analytical models, like those in (3), introduce some imprecision due to constants related to the wing's planform and the 2D airfoil's lift-curve slope. Numerical methods like the Vortex Lattice Method (VLM) provide a more accurate estimation but are computationally intensive. For this project, analytical methods, presented in the equations below are used, which tend to overestimate the lift-curve slope, leading to lower divergence dynamic pressures. This conservative approach ensures safety, and if the calculated divergence speeds remain within the safety margin, numerical refinements may be applied for further improvement. The main analytical models, as presented in (4) and (3) are as follows:

$$c_{l_\alpha} = \frac{a_{2D}(\alpha - \alpha_0)}{1 + \frac{a_{2D}}{\pi e AR}}$$

With  $a_{2D}$  being the lift curve slope of the 2D airfoil (e.g.,  $2\pi$  for thin airfoils),  $AR$  is the aspect ratio,  $\alpha$  is the angle of attack, and  $e$  is the Oswald efficiency factor. For a rectangular wing, the Oswald efficiency factor ( $e$ ) is approximately:

$$e = \frac{1}{1 + \tau}$$

Where  $\tau$  is the span efficiency factor, which accounts for the non-elliptic lift distribution. For rectangular wings,  $\tau \approx 0.05$ . Yet, some alternatives to this equations also considered to have a better overall estimate are:

$$c_{l_\alpha} = C_{L_{2D}} \cdot \frac{AR}{AR + 2}$$

$$c_{l_\alpha} = \frac{C_{L_{2D}}}{\sqrt{1 + \frac{C_{L_{2D}}^2}{\pi^2 AR^2 e^2}}}$$

$$c_{l_\alpha} = \frac{a_{2D}}{1 + \frac{57.3 a_{2D}}{2\pi AR(1+\delta)}}$$

Taking resulting values from this expressions, it is possible to estimate a value for the lift curve slope, to be used in the divergence equations. Finally, if the entire flight envelope stays below the divergence threshold in all configurations, the aircraft can be considered divergence-free.

## 2.2. Flutter analysis

In the pre-design phase, the aerodynamic behavior of the aircraft wing is analyzed using 2D airfoil modeling, focusing on two primary deformation modes: bending and torsion. These modes, typically the most critical in the flutter of a real wing, are represented by two degrees of freedom (DOF): heave, denoted as  $h$  for bending and pitch, denoted as  $\theta$  for torsion. By employing 2D airfoil analysis, the essential flutter characteristics can be captured effectively while significantly reducing the complexity of the problem. A schematic of the 2D airfoil model, illustrating the heaving and pitching motions, is shown in Figure 1. In this figure,  $k_h$  represents the stiffness associated

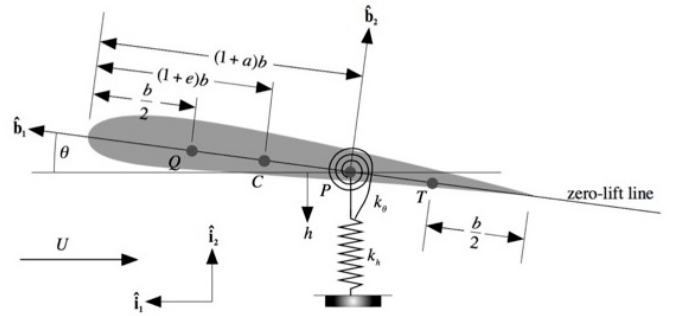


Figure 1: An airfoil cross-section for aeroelastic analysis

with the heaving motion,  $k_\theta$  corresponds to the stiffness associated with the pitching motion,  $Q$  is the aerodynamic center of the wing,  $C$  is the center of mass, and  $P$  denotes the elastic axis of the wing. Additionally,  $b$  is the half-chord length, while  $e$  and  $a$  are parameters indicating the positions of the center of mass and the elastic axis, respectively.

The equation of motion of the airfoil section can be described as:

$$\begin{cases} m\ddot{h} + m b x_\theta \ddot{\theta} + k_h h = -L \\ I_p \ddot{\theta} + m b x_\theta \ddot{h} + k_\theta \theta = M_{ea} \end{cases} \quad (4)$$

where  $m$  is the mass of the wing,  $I_p$  is the moment of inertia of the wing about the elastic axis,  $L$  is the lift force,  $M_{ea}$  is the moment at the elastic axis, and  $x_\theta = e - a$  represents the distance between the center of mass and the elastic axis.

To determine the aeroelastic stability of this system of equations, several methods based on eigenvalue analysis are employed. The methods used in this paper are presented below.

### 2.3. $p$ - $k$ method

The  $p$ - $k$  method (5) is a widely used approach for aeroelastic analysis during the pre-design phase of a new aircraft. It provides accurate information about the flutter velocity and the aeroelastic severity of a given flutter mode. This method combines the advantages and limitations of the  $p$ -method and  $k$ -method (6): the  $p$ -method is used to handle the structural terms, while the  $k$ -method models the unsteady aerodynamic forces.

Mathematically, the system of equations from (4) can be rewritten as a determinant equation:

$$|p^2 \mathbf{M} + \mathbf{K} - \rho_\infty \mathbf{A}(ik)| = 0$$

where  $p$  is the dimensionless eigenvalue,  $k$  is the reduced frequency,  $\mathbf{M}$  is the mass matrix,  $\mathbf{K}$  is the stiffness matrix,  $\mathbf{A}$  is the aerodynamic matrix, and  $\rho_\infty$  is the density of the fluid. Using Theodorsen's unsteady aerodynamic theory (7) to model the aerodynamic terms, the determinant can be written as:

$$\det \begin{pmatrix} p^2 + \frac{\sigma^2}{V^2} - \frac{k^2}{\mu} l_h(k) & p^2 x_\theta - \frac{k^2}{\mu} l_\theta(k) \\ p^2 x_\theta - \frac{k^2}{\mu} m_h(k) & p^2 r^2 + \frac{r^2}{V^2} - \frac{k^2}{\mu} m_\theta(k) \end{pmatrix} = 0 \quad (5)$$

where:

$$\mu = \frac{m}{\pi \rho_\infty b^2 l}, \quad r^2 = \frac{I_p}{mb^2}, \quad V = \frac{U}{b\omega_\theta}, \quad \sigma = \frac{\omega_h}{\omega_\theta},$$

Here,  $\mu$  is the mass ratio,  $r$  is the dimensionless radius of gyration about point  $P$ ,  $\sigma$  is the frequency ratio, and  $V$  is the reduced flow velocity. The terms  $l_h(k)$ ,  $l_\theta(k)$ ,  $m_h(k)$ , and  $m_\theta(k)$  are complex functions of  $k$ , representing the unsteady aerodynamic effects.  $\omega_h$  and  $\omega_\theta$  are the natural frequencies of the heaving and pitching motions, respectively.

The resolution procedure of the  $p$ - $k$  method, as presented in this paper, is outlined below. This method determines the evolution of the reduced frequency  $k$  and the modal damping  $\gamma$  as functions of the reduced velocity  $V$ .

Flutter occurs when modal damping is positive since it indicates that aerodynamic forces are amplifying structural oscillations rather than damping them.

### 2.4. Limitations of the modeling theoretical framework

This model does not account for three-dimensional effects, which are essential for accurately capturing the full aerodynamic behavior of a real wing. By translating the properties of a 3D wing into a 2D airfoil section, we lose some accuracy due to the simplification of airflow interactions. Additionally, while the  $p$ - $k$  method is useful for aeroelastic analysis, it may lead to inaccurate or non-physical results in the post-flutter regime, where the method's assumptions become less valid. These limitations should be considered when interpreting the results.

### Algorithm 1: $p$ - $k$ method resolution procedure

**Input:**  $V_{\text{range}}, \sigma, \mu, r$

**Output:**  $\mathbf{k}, \gamma$

**for each**  $V \in V_{\text{range}}$  **do**

**for each root**  $j \in \{1, 2, 3, 4\}$  **do**

        Initialize  $k^{(0)}$ ;

**for**  $i = 1$  **to**  $n_{\text{iter}}^{\text{max}}$  **do**

            Compute  $\mathbf{M}^{(i-1)}, \mathbf{K}^{(i-1)}, \mathbf{A}^{(i-1)}$  using  $k^{(i-1)}$ ;

            Solve the determinant equation:

$$|p^2 \mathbf{M}^{(i-1)} + \mathbf{K}^{(i-1)} - \rho_\infty \mathbf{A}^{(i-1)}| = 0;$$

            Obtain  $p_j$ , the  $j$ -th root;

$$\text{Compute } k^{(i)} = \text{Re}(p_j) \text{ and } \gamma^{(i)} = \frac{\text{Re}(p_j)}{|\text{Im}(p_j)|};$$

            Check convergence of  $k^{(i)}$  and  $\gamma^{(i)}$ ;

**if convergence achieved then**

**break**;

**return**  $\mathbf{k}, \gamma$

## 3. Model validation

Before utilizing the model, our simulations and computer programs were validated by comparing their results with published data. For  $p$ - $k$  method, our code was validated against results published in (8).

### 3.1. $p$ - $k$ method validation

In the validation case, the parameters are set as :  $a = -\frac{1}{5}$ ,  $e = -\frac{1}{10}$ ,  $\mu = 20$ ,  $r^2 = \frac{6}{25}$ , and  $\sigma = \frac{2}{5}$ . The results obtained using our in-house code are shown in Figures 2 and 4, while the results from (8) are presented in Figures 3 and 5. We observe

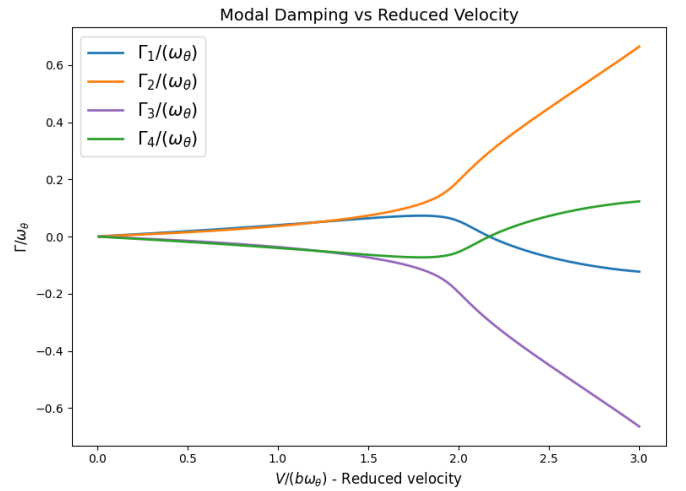


Figure 2: Evolution of the modal damping with respect to the reduced velocity.  $p$ - $k$  method. In house code

that the behavior of the branches is very similar between the results from the book and those obtained using our in-house code. Table 1 presents the flutter frequency and flutter speed obtained with our in-house code, alongside the published results for comparison. We observe that our method produces results similar

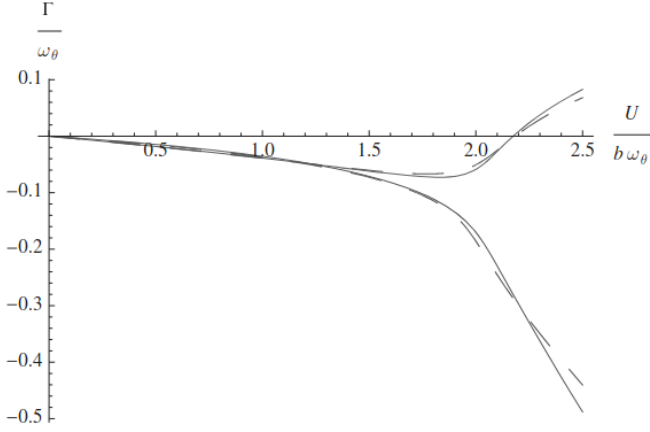


Figure 3: Evolution of the modal damping with respect to the reduced velocity. p-k method. Published results from (8).

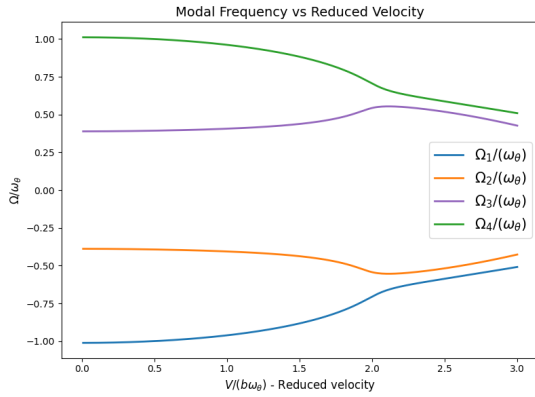


Figure 4: Evolution of the modal frequency with respect to the reduced velocity.  $p - k$  method. In house code

to the published results for both the reduced flutter speed and the reduced flutter frequency.

Table 1: Comparison of reduced flutter frequency and velocity from in-house code and published results

Parameter	In-House res.	Published res.
Reduced flutter Frequency	0.636	0.55
Reduced flutter Speed	2.209	2.18

#### 4. Presentation of the aircraft and flight envelope

The aeroelastic analysis is performed for a general aviation aircraft designed by a Canadian company for operation in Canada and the United States. With a maximum take-off weight of 2200 lbs and powered by a 145 hp piston engine, the aircraft has a 4-hour endurance and a service ceiling of 3 km. Its maximum flight speed is 252 km/h at sea level and 302 km/h at 3 km altitude. The flight envelope of the aircraft is presented in Figure 6.

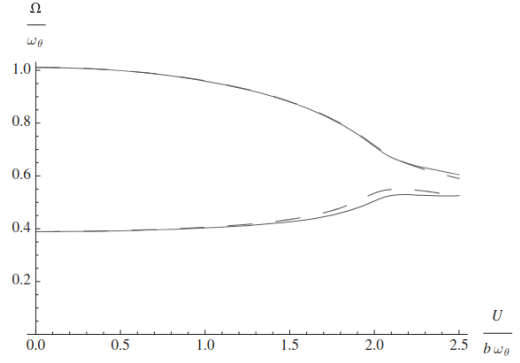


Figure 5: Evolution of the modal frequency with respect to the reduced velocity. p-k method. Published results from (8).

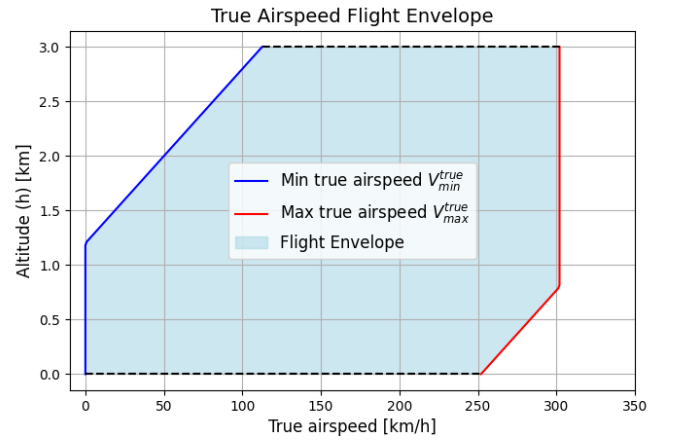


Figure 6: Flight envelope of the aircraft

The empty mass of the wing (excluding fuel tanks) is approximated by  $m_e = 26.91S$ , where  $S$  is the wing area in  $m^2$ . The aircraft has a rectangular wing planform with an area of  $S = 17 m^2$  and an aspect ratio of  $AR = 7.55$ .

Considering the left or right wing, the mass moment of inertia about the elastic axis and the chordwise location of the center of mass change from  $I_p = 7 kg.m^2$  and  $0.35c$  at maximum take-off weight to  $I_p = 4 kg.m^2$  and  $0.45c$  at empty weight, where  $c$  is the chord length. However, the chordwise location of the elastic axis remains unchanged at  $0.4c$ . Each wing carries 80 kg of fuel. The wing has a bending rigidity of  $EI = 2 \times 10^5 N.m^2$  and a torsional rigidity of  $GJ = 10^5 N.m^2$ .

#### 5. Aeroelastic analysis

The aeroelastic analysis consists of four stages: the first stage determines the divergence-free condition of the configuration, the second one, involves a preliminary design assessment to determine whether the initial aircraft design is free from flutter. If flutter is detected, a third stage is conducted to identify the necessary design modifications. The updated design is then reanalyzed to verify whether it is now flutter-free, leading to successive iterations of the design process.

### 5.1. Preliminary Aeroelastic Analysis

In the preliminary analysis, the 2D aerodynamic properties of the aircraft, specifically  $k_\theta$  and  $k_h$ , are derived from the 3D properties of the actual wing. This is achieved by using the uncoupled, circular natural frequencies for both plunge and pitch degrees of freedom (DOF), which are equated to the natural frequencies of the heaving and pitching motions, as follows:

$$\omega_h = (1.8751)^2 \sqrt{\frac{EI}{ml^3}} = \sqrt{\frac{k_h}{m}}$$

$$\omega_\theta = \frac{\pi}{2} \sqrt{\frac{GJ}{I_p l}} = \sqrt{\frac{k_\theta}{I_p}}$$

Also, two extreme cases are defined for the aeroelastic analysis: the fully loaded aircraft at maximum mass and the empty aircraft with no fuel remaining in the wing. These scenarios are analyzed to determine divergence and the maximum and minimum flutter velocities, providing a range within which flutter may occur. The aircraft properties can be determined for each of these two scenarios. These properties are presented below. Table 2 presents the fixed properties of the wing, which remain unchanged regardless of the scenario considered. Table 3 provides the properties for the maximum weight scenario (wing with full fuel), while Table 4 outlines the properties for the minimum weight scenario (empty wing).

Table 2: Fixed Aircraft Properties

Property	Symbol	Value
Wing area (whole wing)	$S$	17.00 m <sup>2</sup>
Aspect ratio	$AR$	7.55
Span (right/left wing)	$l$	5.66 m
Chord length	$c$	1.50 m
Half-chord	$b$	0.75 m
Bending rigidity	$\overline{EI}$	$2.00 \times 10^5$ N·m <sup>2</sup>
Torsional rigidity	$\overline{GJ}$	$1.00 \times 10^5$ N·m <sup>2</sup>
Elastic axis location	$a$	-0.20
Empty mass (whole wing)	$m_e$	457.47 kg
Max. mass of fuel (right/left)	$m_{\text{fuel}}$	80.00 kg

Table 3: Scenario-Dependent Properties : Maximum Weight Scenario

Property	Symbol	Value
Mass (right/left wing)	$m_{\text{max}}$	308.74 kg
Center of mass location	$e_{\text{max}}$	-0.30
Mass moment of inertia	$I_{p,\text{max}}$	7.00 kg·m <sup>2</sup>
Heaving natural frequency	$\omega_{h,\text{max}}$	6.64 rad/s
Pitching natural Frequency	$\omega_{\theta,\text{max}}$	78.88 rad/s

### 5.2. Divergence Analysis

Recalling equation 3, the divergence dynamic pressure depends on the wing's cross-sectional torsional stiffness, chord

Table 4: Scenario-Dependent Properties : Empty Wing Scenario

Property	Symbol	Value
Mass (right/left wing)	$m_{\text{min}}$	228.74 kg
Center of mass location	$e_{\text{min}}$	-0.10
Mass moment of inertia	$I_{p,\text{min}}$	4.00 kg·m <sup>2</sup>
Plunging natural frequency	$\omega_{h,\text{min}}$	7.71 rad/s
Pitching natural frequency	$\omega_{\theta,\text{min}}$	104.35 rad/s

length, lift-curve slope, and the distance between the elastic axis and aerodynamic center. As shown in section 4, all these parameters remain constant across the two cases. Therefore, a single analysis, independent of the scenario, is sufficient.

As introduced in the theoretical analysis, the lift-curve slope may be estimated through numerous analytical approaches, as the ones presented in (3) or (4). Overall, for the fixed aircraft properties, being the aspect ratio, chord, span, and the rectangular platform, this value can be averaged around  $4.5 \text{ rad}^{-1}$ . Using the parameters defined in the table above, the divergence dynamic pressure can be expressed as:

$$q_D = \left(\frac{\pi}{2l}\right)^2 \frac{\overline{GJ}}{cc_{l_\alpha} b \left(a + \frac{1}{2}\right)} = 5071.31 \text{ [Pa]}$$

The dynamic divergence pressure can be converted into a divergence speed as:

$$V_D = \sqrt{\frac{2q_D}{\rho_\infty}}$$

The variation of air density with altitude is described using the International Standard Atmosphere (9) model as follows:

$$\rho(h) = \rho_0 \left( \frac{T_0 - 0.0065h}{T_0} \right)^{\frac{g}{0.0065R} - 1}$$

where  $\rho_0 = 1.225 \text{ kg/m}^3$  is the air density at sea level,  $T_0 = 288.15 \text{ K}$  is the reference temperature at sea level,  $h$  is the altitude in  $m$ ,  $g = 9.81 \text{ m/s}^2$  is the gravity acceleration,  $R = 287.06 \text{ J/(kg.K)}$  is the specific air constant and  $0.0065 \text{ K/m}$  is the temperature gradient. Therefore, the divergence speed is a function of altitude  $h$ .

Figure 7 shows the flight envelope along with the corresponding divergence speed for each altitude  $h$ . It can be observed that while the divergence speeds lie outside the effective flight envelope, they remain within the 15% margin zone at an altitude of approximately 1 km. Consequently, design modifications will be required to ensure compliance with the regulations.

### 5.3. Flutter Analysis

To determine whether the aircraft is flutter-free across its entire flight envelope, the following procedure is used: for each altitude, the minimum and maximum speeds of the aircraft are derived from the flight envelope definition in Figure 6. This defines the range of aircraft velocities. From this, the range of reduced flutter velocities to be studied is determined. The analysis must be performed for each altitude  $h$ , as air density

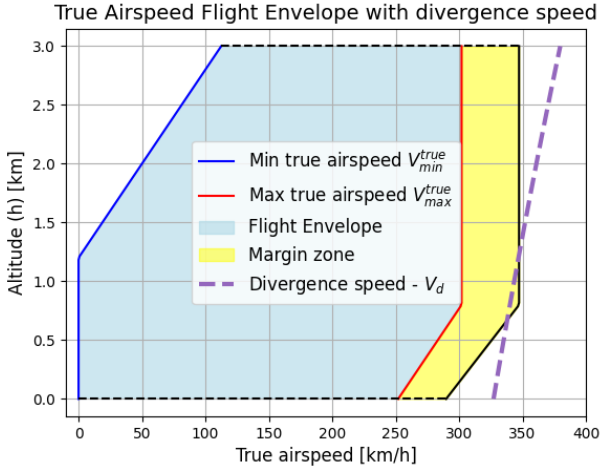


Figure 7: Flight envelope with divergence speed and margin zone for the initial design

changes with altitude. This introduces a dependence of the non-dimensional coefficient  $\mu$  on altitude, which, in turn, affects the aircraft's flutter speed. According to the regulations, an aircraft is considered flutter-free if and only if its lowest flutter speed is greater than or equal to 1.15 times the maximum aircraft speed, as defined by its flight envelope.

The results from the analysis are presented in Figure 8. It is observed that for the maximum weight scenario, the flutter speed is well above the regulatory margin zone, indicating that this scenario does not represent a critical concern for the aeroelasticity of the aircraft. However, for the minimum weight scenario, the flutter speed falls within or near the margin zone of the flight envelope, depending on the altitude. This condition is unacceptable, necessitating a redesign of the aircraft to ensure it remains free from flutter under all operational conditions. Although it is highly improbable for the aircraft to fly with no fuel in the wing, this scenario serves as a conservative design approach, providing an additional safety margin for the aeroelastic design of the aircraft by considering this extreme case. To gain

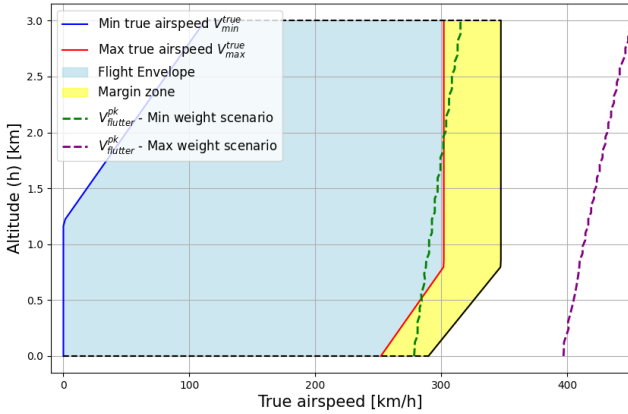


Figure 8: Flight envelope with flutter speed and margin zone for the initial design

insights into the flutter behavior in the minimum weight scenario, the evolution of the modal frequency and modal damping with respect to the reduced velocity is analyzed for an altitude of  $h=1.5$  km. Results are presented in Figures 9 and 10. It is observed that the flutter is primarily induced by the heaving motion, as indicated by the modal frequency. Furthermore, the modal damping analysis shows that the flutter is not of high severity, which is advantageous for the aircraft's redesign process.

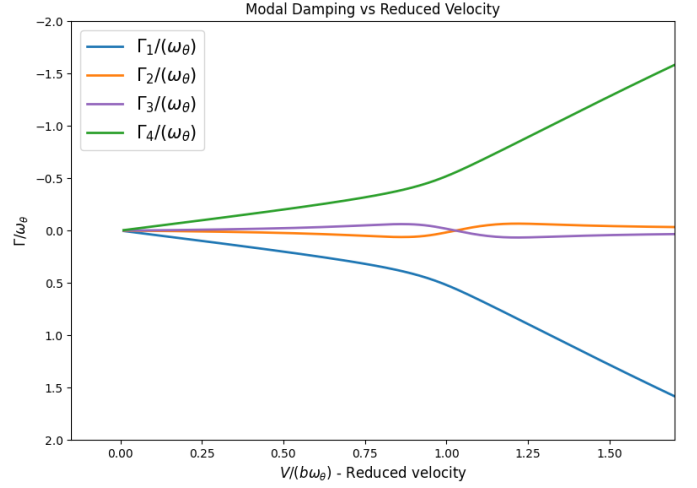


Figure 9: Evolution of modal damping with respect to the reduced velocity. Empty wing scenario at  $h = 1.5$  km. p-k method

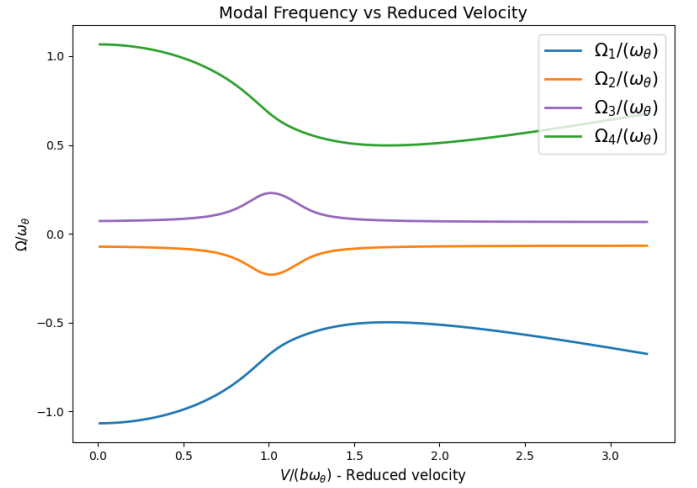


Figure 10: Evolution of modal frequency with respect to the reduced velocity. Empty wing scenario at  $h = 1.5$  km. p-k method

#### 5.4. Design modifications

To guarantee a flutter-free design in the empty wing scenario, design modifications are required. To determine appropriate design modifications, we first analyzed the parameters that vary between the maximum weight wing scenario and the empty wing scenario. This analysis identified four non-dimensional

Table 5: Values of non-dimensional parameters for both scenarios at  $h = 1.5km$ 

Parameter	Empty wing	Max weight
Mass ratio, $\mu$	21.58	29.13
Frequency ratio, $\sigma$	0.074	0.0841
Radius of gyration, $r^2$	0.0311	0.0403
Center of mass to elastic axis, $x_\theta$	0.1	-0.1

parameters that change:  $\mu$ ,  $r^2$ ,  $\sigma$ , and  $x_\theta$ . Consequently, a parametric study is performed to examine the influence of these coefficients on the reduced flutter velocity. For each of the parameters, the analysis is conducted while assuming that all other parameters remain constant, though this assumption may not hold in all cases. The analysis is performed considering an altitude  $h = 1.5km$ . Table 5 summarizes the values of the non-dimensional parameters for the two extreme scenarios at the specified altitude.

Figure 11 illustrates the influence of the mass ratio,  $\mu$ , on the reduced flutter velocity. The analysis reveals that an increase in the mass ratio leads to a corresponding rise in the flutter velocity. This observation aligns with the results of the preliminary analysis, where the flutter velocity was significantly higher for the maximum weight scenario compared to the empty wing scenario.

Figure 12 illustrates the influence of the dimensionless radius of gyration on the reduced flutter velocity. An increase in the radius of gyration results in a higher reduced flutter velocity.

Figure 13 illustrates the influence of  $x_\theta$  on the reduced flutter velocity. Among the parameters analyzed,  $x_\theta$  exhibits the most significant impact on the reduced flutter velocity. Referring to Table 5, it is evident that in the empty wing scenario,  $x_\theta$  is positive, indicating that the center of mass is positioned behind the elastic axis. This configuration has a destabilizing effect on the wing's aeroelastic stability.

For the frequency ratio analysis, it has been shown that this parameter has a minimal effect on the wing's flutter velocity. As a result, we do not present it here, as its influence is negligible in the context of our aeroelastic stability study.

As a conclusion, the results from the parametric analysis reveal the following trends: increasing the mass ratio leads to a higher reduced flutter velocity, as does an increase in the radius of gyration. Additionally, reducing  $x_\theta$  (the distance between the center of mass and the elastic axis) also contributes to an increase in the reduced flutter velocity.

Since it was shown that  $x_\theta$  was found to have the greatest influence on the reduced flutter velocity, our design modifications should prioritize adjustments to this parameter. To improve the aeroelastic stability and move the center of mass ahead of the elastic axis, several design modifications can be considered. One option is to add a mass at the wing's leading edge. Installing a weight near the tip or forward section of the wing can shift the center of mass forward. This method is simple and can be implemented without major changes to the existing wing structure. However, the added weight could increase the aircraft's overall weight, which may reduce fuel efficiency.

A second option involves using a lighter material for the rear wing structure. By replacing some of the rear wing's components with lightweight materials, such as composites, the mass at the tail section is reduced, helping to reposition the center of mass forward. This change not only improves stability but also enhances overall aircraft performance. However, this approach may increase the cost of materials, and the integration of advanced materials could complicate the design and manufacturing processes while still meeting structural integrity requirements.

Lastly, repositioning internal components, such as fuel tanks or avionics, can also help. This approach is relatively inexpensive during the design phase of the aircraft. However, for existing aircraft designs, it may be impractical or difficult without major modifications to other systems. Furthermore, shifting internal components might affect the aircraft's overall balance, requiring adjustments in other parts of the design.

We have chosen to use lighter materials in the rear wing structure to shift the center of mass forward and improve the aircraft's flutter stability. This decision offers several advantages and disadvantages.

The main benefit of using lighter materials for the rear is the reduction in the overall mass of the aircraft. By using advanced composites or high-strength, lightweight alloys in the rear wing structure, we can reduce the overall weight. This results in better fuel efficiency, less structural stress on the wing's attachment points, and enhanced stability, as the aircraft will have a more favorable distribution of mass.

However, there are significant drawbacks to using these lighter materials. One of the primary concerns is the higher cost. Advanced materials such as carbon fiber composites or titanium alloys are considerably more expensive than traditional materials like aluminum, yet, the current efforts of the industry to transition to more sustainable operations, has drawn massive improvements regarding the adoption of this materials. On the other hand, while the manufacturing processes is significantly more complex and require specialized equipment, which further drives up the cost of production, has been a focus of research and development among the current leading companies and innovation centres worldwide, developments on manufacturing techniques have made possible almost doubling the composite structural weight. Additionally, the testing, certification, and quality assurance processes for these advanced materials can add to the overall expense.

Despite these higher costs, the decision to use lighter materials in the rear wing structure is justified by the performance improvements and regulatory pressures towards reducing the environmental impact of aircraft. By reducing the weight and improving fuel efficiency, this modification will contribute to long-term operational savings, even though the initial investment is higher.

We assume that this design modification leads to a 20% reduction in mass and mass moment of inertia, with the center of mass shifting from 0.35c to 0.28c for the maximum weight scenario and from 0.45c to 0.38c for the empty wing scenario. Additionally, we assume that the rigidity of the rear wing structure, represented by the bending stiffness  $EI$  and torsional stiffness



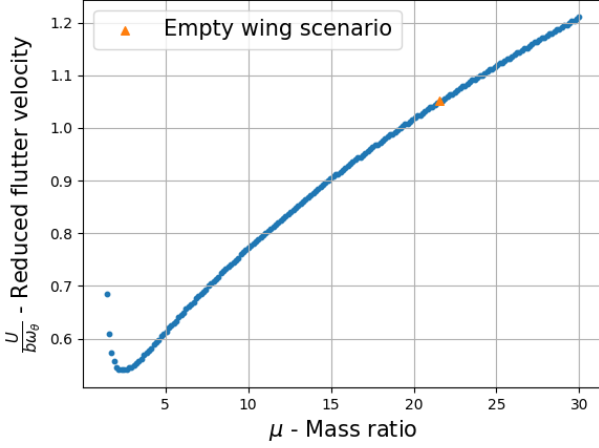


Figure 11: Effect of mass ratio  $\mu$  on reduced flutter velocity

$\overline{GJ}$ , is increased by 15% due to the use of high-performance materials. These assumptions, including the mass reduction, inertia reduction, the shifting of the center of mass, and the increase in rigidity, depend heavily on the materials selected and should be validated once the specific materials are chosen. To

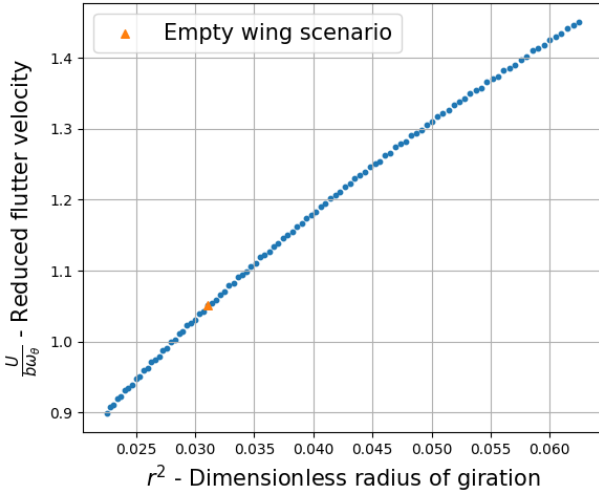


Figure 12: Effect of dimensionless radius of gyration  $r$  on reduced flutter velocity

validate our design modifications, a new flutter analysis is conducted using the  $p - k$  method. Since the preliminary analysis identified the empty wing scenario as the critical case, computations are focused exclusively on this configuration. Figure 14 illustrates the flight envelope alongside the flutter boundary for the modified design in the empty wing configuration. It can be observed that, at every altitude  $h$ , the flutter velocity exceeds 1.15 times the maximum flight speed of the aircraft at that altitude, thereby complying with regulatory requirements. Figure 15 presents the flight envelope with the divergence speed at each altitude  $h$ . It can be observed that at all altitudes, the

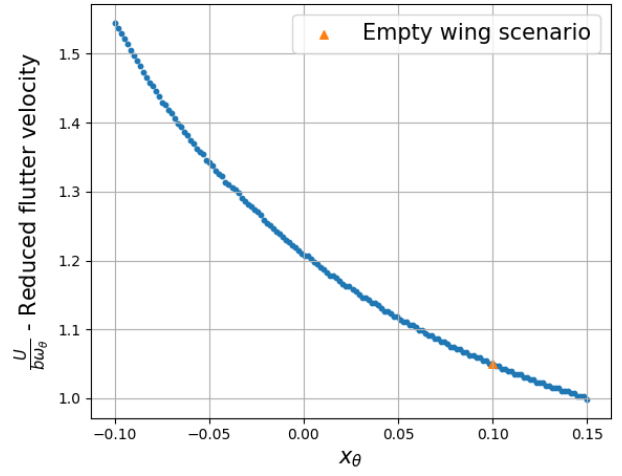


Figure 13: Effect of  $x_\theta$  on reduced flutter velocity

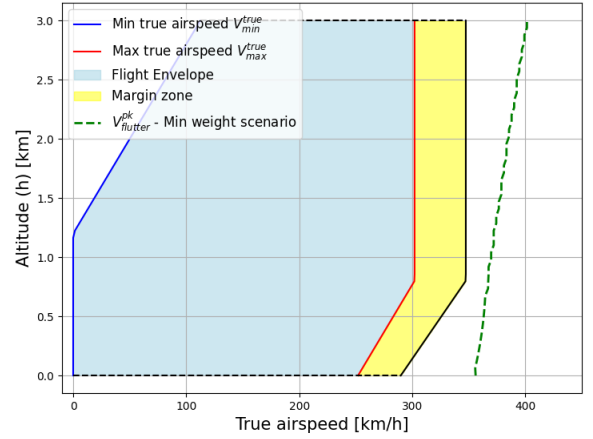


Figure 14: Flight envelope with flutter speed and margin zone for the modified design

divergence speed falls outside the 15% margin zone, ensuring compliance with the regulations.

## 6. Electric Aircraft Analysis

To determine the feasibility of an electric version of this aircraft, a comparative analysis is conducted, considering the respective design considerations and their impact on aeroelastic performance using the same analysis method.

First, the modifications required to transition from an internal combustion propulsion system to an electric propulsion system are identified. Through this comparative analysis, it is determined whether the aircraft can meet its operational expectations or if these need to be adjusted for feasibility in terms of endurance and required shaft power.

Subsequently, based on these characteristics, new input parameters are defined to perform the flutter analysis using the



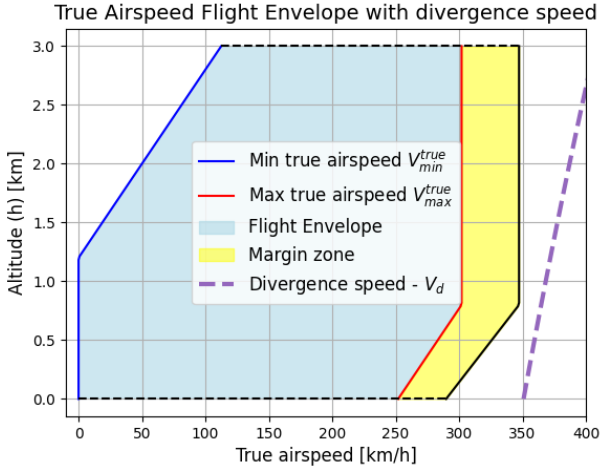


Figure 15: Flight envelope with divergence speed and margin zone for the modified design

p-k method and verify compliance with certification criteria.

Finally, the short- and long-term advantages of incorporating an electric version of the aircraft to make up to 50% of the company's 400-airplane fleet are discussed. This includes evaluating the economic and environmental impacts of its operation in an interval of 1 to 10 years.

#### 6.1. Design analysis of the electric aircraft

The transition to an electric propulsion system primarily impacts the total mass of the aircraft and its distribution due to the different weights of the engine and the disparity between the fuel weight and the batteries required to supply the total energy demanded by the system.

Given that the piston engine produces a power output of 145 hp (approximately 106.647 kW) with a total operating time of 4 hours, the maximum energy consumption can be determined as:

$$106.647 \text{ kW} \times 4 \text{ h} = 426.588 \text{ kWh}$$

While inefficiencies in energy production and utilization exist, these can be neglected for this simplified analysis since electric motors are highly efficient, and this study focuses on general sizing considerations.

Despite significant advancements in the specific energy of batteries for electric aviation, the current market average is 250-300 Wh/kg (10). Thus, to achieve the same energy level, a battery pack weighing approximately 1450 kg (3196.7 lb) would be required.

Meanwhile, a 145 hp piston engine, such as the Continental O-300 or the C145, both built by Continental Motors Company (11), can weigh approximately 120 kg. Whereas an electric version can be between 15 and 30 kilograms.

This means the total estimated weight of the electric propulsion system is around 3250 lb, compared to the 620 lb of the internal combustion system. This represents a significant increase and imposes an operational limit, as it exceeds the aircraft's MTOW of 2200 lb. Since the objective is to create a

variant of the aircraft rather than a complete redesign, feasibility depends on limiting the operational capabilities, such as the aircraft's endurance. This constraint explains why electric aircraft are currently used primarily for short routes until new developments enable specific energy values closer to those of fossil fuels.

To establish the possible endurance of the electric version, the weight of the electric system can be limited to match the combustion system (620 lb), approximately 28.2% of the MTOW.

Assuming the motor weighs approximately 60 lb, this leaves 560 lb (254 kg) for the batteries. Using the same specific energy factor of 300 Wh/kg, this equates to a total energy of 76.2 kWh. Consequently, for a power output of approximately 106 kW, the flight time is estimated to be 40-45 minutes, aligning with current values for electric aircraft as shown in (12).

Regarding the parameters for the aeroelastic analysis, as mentioned earlier, since the electric configuration is only a variant, most structural and aerodynamic descriptors can be assumed invariant, except for those strongly related to the wing's total mass and its distribution. However, to simplify the case study, it is assumed that the bending and torsional rigidity will remain unchanged, and that the mass moment of inertia and the center of gravity will vary proportionally to the weight of the wing by the following expressions, in terms of  $m_{max}$ , the combined weight of the wing and the batteries inside.

$$I_p = 0.0375 \times m_{max} - 4.57775$$

$$e_{max} = -0.6667 \times \ln(m_{max}) + 3.5202$$

#### 6.2. Aeroelastic analysis of the electric aircraft

As the fixed parameters of the aircraft concerning divergence remain unchanged. It can be safely determined that this configuration is also complying with the regulations regarding this phenomena.

For the flutter analysis, following a procedure analogous to the one previously conducted for the piston-engine-powered version of the aircraft, using the validated p-k method, the corresponding values of  $\omega_h$  and  $\omega_\theta$  are derived.

Since the weight of the batteries does not change significantly whether they are charged or discharged, the concept of maximum and empty weight previously analyzed does not apply. Instead, the weight variation depends on the fraction of the batteries stored in the wings versus the fuselage, affecting the dynamic stability of the aircraft. However, since the case with all the batteries in the fuselage corresponds to the *Empty Weight Scenario* (Table 4), an analysis is conducted for a configuration where all the batteries are located in the wings. Additionally, a scenario that just meets the safety margin is considered, establishing a design limitation regarding the weight distribution of the batteries.

The fixed electric aircraft properties and the scenario-dependent properties for both cases are presented in Tables 6, 7, and 8.

The results for the case with all the batteries located inside the wing are presented in Figure 16. As expected, the increased

Table 6: Fixed Electric Aircraft Properties

Property	Symbol	Value
Wing area (whole wing)	$S$	17.00 m <sup>2</sup>
Aspect ratio	$AR$	7.55
Span (right/left wing)	$l$	5.66 m
Chord length	$c$	1.50 m
Half-chord	$b$	0.75 m
Bending rigidity	$\overline{EI}$	$2.00 \times 10^5$ N·m <sup>2</sup>
Torsional rigidity	$\overline{GJ}$	$1.00 \times 10^5$ N·m <sup>2</sup>
Elastic axis location	$a$	-0.20
Empty mass (whole wing)	$m_e$	457.47 kg

Table 7: Scenario-Dependent Properties : All batteries in wings

Property	Symbol	Value
Mass of batteries (right/left)	$m_{bat}$	127 kg
Mass (right/left wing)	$m_{max}$	355.735 kg
Center of mass location	$e_{max}$	-0.396
Mass moment of inertia	$I_{p,max}$	8.76 kg·m <sup>2</sup>
Heaving natural frequency	$\omega_{h,max}$	6.18 rad/s
Pitching natural Frequency	$\omega_{\theta,max}$	70.50 rad/s

mass and location of the center of mass with respect to the elastic axis, yields a stable configuration, with a characteristic flutter velocity significantly above the maximum flight speed at all flight levels, therefore confirming the compliance with the flutter-free condition regulations.

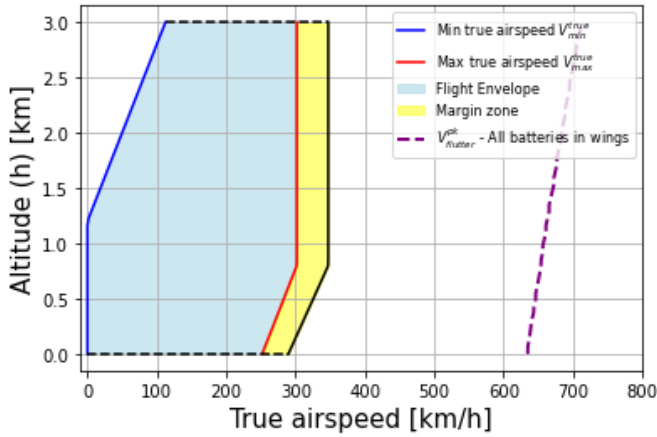


Figure 16: Flight envelope with flutter speed and margin zone for the electric version with all the batteries in the wing

Then, through the iterative analysis, it is found that at least 40% of  $m_{bat}$  (50.8 kg) must be placed on each wing to comply with the safety margin, if the center of mass location is proportional to the total mass of the wing, as it was defined. The corresponding results are presented in Figure 17.

For both scenarios, the roots at  $h = 1.5$  km, behave similarly to the combustion engine configuration. As the second situation is more critical, the respective modal damping and frequency evolution with the increasing reduced velocity are presented in

Table 8: Scenario-Dependent Properties : Batteries in wing design limit

Property	Symbol	Value
Mass of batteries in wing (right/left)	$m_{bmin}$	50.8 kg
Mass (right/left wing)	$m_{min}$	279.535 kg
Center of mass location	$e_{min}$	-0.235
Mass moment of inertia	$I_{p,min}$	5.90 kg·m <sup>2</sup>
Plunging natural frequency	$\omega_{h,min}$	6.97
Pitching natural frequency	$\omega_{\theta,min}$	85.88

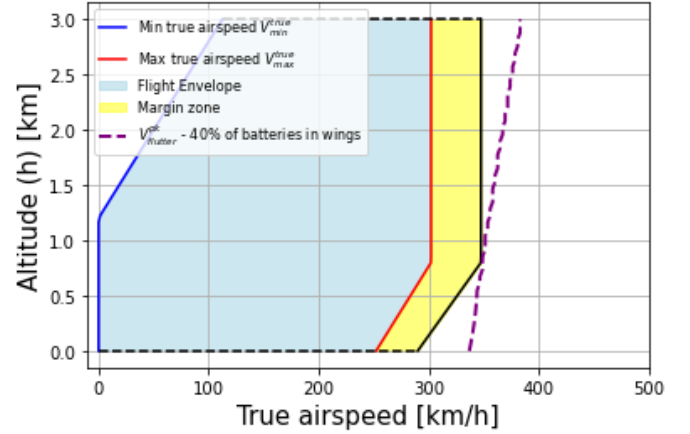


Figure 17: Flight envelope with flutter speed and margin zone for the electric version with 40% of the batteries in the wing

Figures 18 and 19, revealing the stable nature of the model until the identified flutter onset.

While the results may provide some insight into the nature of flutter for this aircraft, it has to be noted that the configuration is highly sensitive to the location of the center of mass with respect to the elastic axis  $x_\theta$ , and that significant assumption on the relation between the total mass of the wing and the location of the center of mass were made. Thus, while the current study provides a valuable first assessment, latter analysis will be required as the design process advances and the model descriptors are refined.

### 6.3. Environmental and economic impact of an electric version

The adoption of all-electric aircraft propulsion systems is becoming an increasingly viable solution for reducing the environmental impact of aviation due to technological advancements. In this section, we evaluate the short-term (1 year) and long-term (10 years) environmental and economic impacts of converting a conventional piston-engine aircraft into an all-electric version. Several key assumptions were made for this analysis:

- The energy consumption of the electric motor is assumed to be more efficient than the piston engine, with an efficiency of approximately 90% for the electric version compared to 30% for the piston engine.
- The cost of electricity is \$0.15 per kWh (13), while the cost of aviation gasoline (Avgas) is \$1.60 per liter (14).

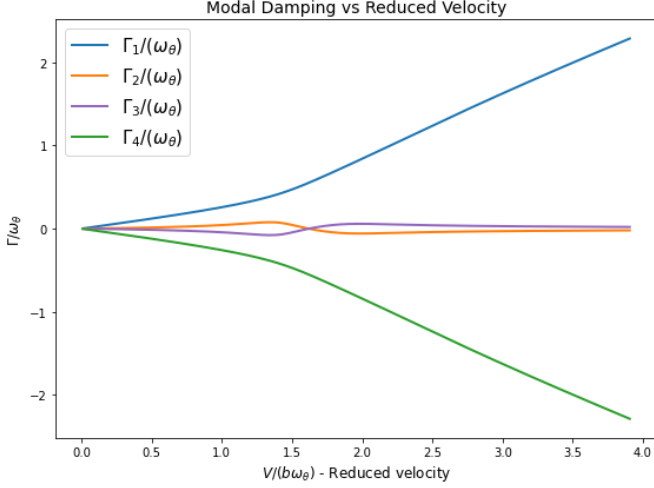


Figure 18: Evolution of modal damping with respect to the reduced velocity. Distributed batteries scenario at  $h = 1.5\text{km}$ . p-k method

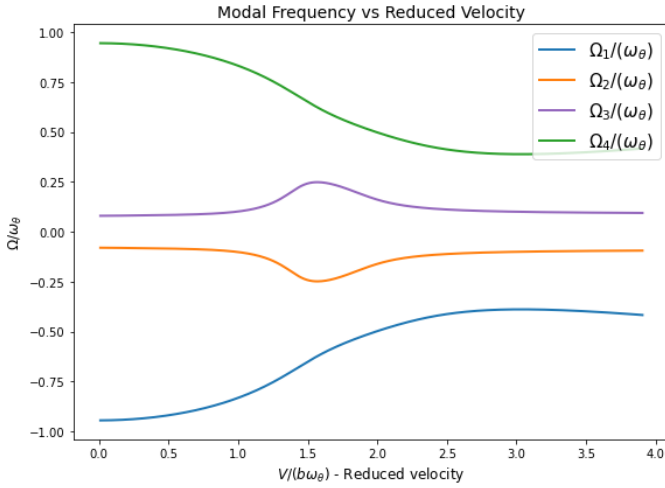


Figure 19: Evolution of modal frequency with respect to the reduced velocity. Distributed batteries scenario at  $h = 1.5\text{km}$ . p-k method

- The environmental impact of electricity generation in Canada is assumed to be  $0.1 \text{ kg CO}_2 \text{ per kWh}$  (13), due to the country's reliance on clean energy.
- The annual flight time is assumed to be 300 flight hours for both versions of the aircraft.

### 6.3.1. Short-term environmental and economic impacts

In this subsection, we analyze the short-term environmental impact of converting a conventional piston-engine aircraft into an all-electric version. For the environmental effect, the differences in  $\text{CO}_2$  emissions over one year for both versions are compared.

**Piston-engine Version.** The  $\text{CO}_2$  emissions over one year of a piston engine aircraft are estimated. Let:

- $P_{\text{hp}}$  be the power output of the piston engine in horsepower (145 hp),

- $P_{\text{kW}}$  be the power output in kilowatts,
- $\eta_{\text{piston}}$  be the efficiency of the piston engine (0.30),
- $E_{\text{fuel}}$  be the total energy consumption in kilowatt-hours per year,
- $V_{\text{fuel}}$  be the total volume of fuel consumed in liters per year,
- $\rho_{\text{fuel}}$  be the density of Avgas fuel (2.33 kg/L),
- $\text{CO}_2^{\text{fuel}}$  be the total  $\text{CO}_2$  emissions in kilograms per year,
- $S$  be the number of flights per year (300 flights),
- $T_{\text{flight}}$  be the duration of each flight (4 hours).

First, the power output of the piston engine in kilowatts is given by the conversion factor  $1 \text{ hp} = 0.7355 \text{ kW}$ :

$$P_{\text{kW}} = P_{\text{hp}} \times 0.735 = 106.58 \text{ kW}$$

The energy consumption of the piston engine over a year is then calculated by multiplying the power by the total flight time for the year, considering the efficiency of the piston engine:

$$E_{\text{fuel}} = P_{\text{kW}} \times T_{\text{flight}} \times S / \eta_{\text{piston}} = 426,320 \text{ kWh/year}$$

The volume of fuel consumed per year, using the energy density of Avgas  $\varepsilon_{\text{fuel}} = 33.41 \text{ kWh/L}$ :

$$V_{\text{fuel}} = \frac{E_{\text{fuel}}}{\varepsilon_{\text{fuel}}} = \frac{426,320 \text{ kWh/year}}{33.41 \text{ kWh/L}} = 12,760 \text{ L/year}$$

The  $\text{CO}_2$  emissions for the piston-engine version are calculated by multiplying the volume of fuel by the emission factor  $\rho_{\text{fuel}} = 2.33 \text{ kg/L}$ :

$$\text{CO}_2^{\text{fuel}} = V_{\text{fuel}} \times \rho_{\text{fuel}} = 29,731.4 \text{ kg CO}_2/\text{year}$$

**Electric Version.** The  $\text{CO}_2$  emissions over one year of an all electrical aircraft are estimated. Let:

- $E_{\text{electric}}$  be the total energy consumption in kilowatt-hours per year for the electric version,
- $\eta_{\text{electric}}$  be the efficiency of the electric motor (90% or 0.90),
- $\rho_{\text{electric}}$  be the  $\text{CO}_2$  intensity of electricity generation ( $0.1 \text{ kg CO}_2/\text{kWh}$ ).

For the electric version, we assume that the power required for flight is the same as in the piston-engine version, so the energy consumption remains the same. However, due to the higher efficiency of the electric motor, the energy use is reduced by a factor of  $\eta_{\text{electric}}$ :

$$E_{\text{electric}} = P_{\text{kW}} \times T_{\text{flight}} \times S / \eta_{\text{electric}} = 142,106 \text{ kWh/year}$$

Next, the  $\text{CO}_2$  emissions for the electric version are calculated by multiplying the total energy consumption by the  $\text{CO}_2$  intensity  $\rho_{\text{electric}} = 0.1 \text{ kg CO}_2/\text{kWh}$ :

$$\text{CO}_2^{\text{electric}} = E_{\text{electric}} \times \rho_{\text{electric}} = 14,210.6 \text{ kg CO}_2/\text{year}$$

*Net Reduction in CO<sub>2</sub> Emissions.* Therefore, the net reduction in CO<sub>2</sub> emissions when switching from the piston-engine version to the electric version can be obtained :

$$\Delta\text{CO}_2^{1\text{ year}} = \text{CO}_2^{\text{fuel}} - \text{CO}_2^{\text{electric}} = 15,520 \text{ kg CO}_2$$

This result indicates that the all-electric version of the aircraft would lead to a reduction in CO<sub>2</sub> emissions, owing to the higher efficiency of the electric motors compared to conventional piston engines. However, it is important to note that this analysis does not account for the CO<sub>2</sub> emissions associated with the production of electric batteries. The manufacturing process for electric batteries, particularly lithium-ion batteries, involves significant energy consumption and CO<sub>2</sub> emissions. Additionally, the extraction and processing of raw materials for these batteries, such as lithium, cobalt, and nickel, can have serious environmental and social implications (15). These materials are often sourced from regions where mining operations can cause habitat destruction, water pollution, and exploitation of labor. Moreover, the demand for these rare materials is increasing, which can lead to resource depletion and greater geopolitical tensions. Therefore, while electric aircraft may offer environmental benefits in terms of operational emissions, the full life-cycle impact of battery production and material sourcing must also be considered to understand the broader environmental and social consequences.

The economic impact are now considered. For the piston-engine version of the aircraft, the annual fuel cost can be calculated by multiplying the total fuel consumption of 12,760 liters per year by the price of fuel, which is assumed to be 1.60 \$/L. This yields the following fuel cost per year:

$$\text{Fuel cost} = 12,760 \text{ L/year} \times 1.60 \text{ $/L} = 20,416 \text{ $/year}$$

For the all-electric version, the annual electricity cost is calculated by multiplying the total energy consumption of 142,106 kWh per year by the electricity price, which is assumed to be 0.15 \$/kWh. This results in the following electricity cost per year:

$$\text{Electricity cost} = 21,315 \text{ $/year}$$

Therefore, we observe that the annual operating costs of the electric version are fairly comparable to those of the conventional piston-engine version, with the fuel-powered version incurring slightly lower costs. However, this analysis does not consider maintenance costs for the motors, batteries or other operational factors, which, while challenging to quantify, are essential for a comprehensive assessment. In the short term, these maintenance costs are expected to be negligible.

#### 6.4. Long-Term (10-Year) Environmental and Economic Impacts

Over 10 years, assuming the same operational patterns, the total CO<sub>2</sub> reduction is:

$$\Delta\text{CO}_2^{10\text{ year}} = \Delta\text{CO}_2^{1\text{ year}} \times 10 = 155,200 \text{ kg CO}_2$$

*Economic Impact.* The long-term economic impact takes into account not only the annual operational costs but also additional factors such as battery replacement and potential infrastructure investments.

*Piston-engine Version.* The annual fuel cost for the piston-engine version over 10 years can be calculated as follows:

$$\text{Fuel cost (10 years)} = 20,416 \text{ $/year} \times 10 = 204,160 \text{ $}$$

*Electric Version.* For the electric version, the annual electricity cost is 21,315 \$/year, leading to the following electricity cost over 10 years:

$$\text{Electricity cost (10 years)} = 21,315 \text{ $/year} \times 10 = 213,150 \text{ $}$$

One of the key considerations for the electric aircraft over the long term is the need for battery replacement. Assuming that the battery has a lifespan of 5 years, the electric aircraft would require two full battery replacements over the 10-year period. If the cost of a battery is estimated at 100,000\$ per battery, the total cost of battery replacements over 10 years would be:

$$\text{Battery replacement cost} = 2 \times 100,000 \text{ $} = 200,000 \text{ $}$$

The total operating costs for the electric version over 10 years, including the electricity cost and battery replacement, are therefore:

$$\text{Total operating cost (10 years)} = 413,150 \text{ $}$$

Therefore, the net increase in operating costs for the electric version over 10 years, compared to the piston-engine version, is:

$$\text{Net increase in operating costs} = 208,990 \text{ $}$$

This indicates that, while the electric version offers long-term environmental benefits, the total operating costs over 10 years are significantly higher due to the cost of battery replacements. Additionally, factors such as infrastructure investment for charging stations and potential maintenance of electric motors could further increase the long-term costs. It should be noted that our analysis neglect the cost associated with the maintenance of the piston-engines that are expected to be negligible. Overall, the long-term analysis highlights the trade-offs between environmental and economic impacts. The electric aircraft provides substantial reductions in CO<sub>2</sub> emissions, but the higher operating costs, particularly due to battery replacement and infrastructure needs, must be considered in any long-term economic assessment.

## 7. Bonus : Multi degree of freedom analysis

In this section, the wing is modeled as an unswept structure with uniform properties and is idealized as a clamped-free beam. The beam is assumed to undergo either torsion or bending, but not in a coupled manner. The transverse displacement of the beam is denoted as  $w(y)$ , while the pitching degree of freedom is represented by  $\theta(y)$ . A schematic representation of

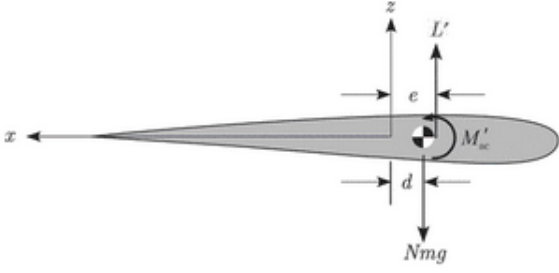


Figure 20: Schematic of the situation

the problem is shown in Figure 20. For a uniform wing, the potential energy  $PE$  is expressed as the strain energy stored in the structure due to both bending and torsional deformations:

$$PE = \frac{1}{2} \int_0^L \iint_{A(y)} \left[ EI \left( \frac{\partial^2 w}{\partial y^2} \right)^2 + GJ \left( \frac{\partial \theta}{\partial y} \right)^2 \right] dA dy \quad (6)$$

The velocity of an arbitrary point  $P(x, z)$  at the wing section is defined as:

$$\vec{v} = z \frac{\partial \theta}{\partial t} \vec{i} + \left[ \frac{\partial w}{\partial t} - x \frac{\partial \theta}{\partial t} \right] \vec{k}$$

where  $\vec{i}$  and  $\vec{k}$  are unit vectors in the  $x$  and  $z$  directions. Therefore, the kinetic energy ( $KE$ ) can be expressed as :

$$KE = \frac{1}{2} \int_0^L \iint_{A(y)} \rho \left[ z^2 \left( \frac{\partial \theta}{\partial t} \right)^2 + \left( \frac{\partial w}{\partial t} - x \frac{\partial \theta}{\partial t} \right)^2 \right] dA dy \quad (7)$$

This can be reformulated as :

$$KE = \frac{1}{2} \int_0^L \iint_{A(y)} \rho \left[ r^2 \left( \frac{\partial \theta}{\partial t} \right)^2 + \left( \frac{\partial w}{\partial t} \right)^2 - 2x \frac{\partial w}{\partial t} \frac{\partial \theta}{\partial t} \right] dA dy$$

where  $r$  is the distance of the point  $P$  to the elastic axis. By expanding the cross-sectional integral, the kinetic energy is expressed as:

$$KE = \frac{1}{2} \int_0^L \left[ m \left( \frac{\partial w}{\partial t} \right)^2 + mb^2 r^2 \left( \frac{\partial \theta}{\partial t} \right)^2 - 2mbx_\theta \frac{\partial w}{\partial t} \frac{\partial \theta}{\partial t} \right] dy \quad (8)$$

Finally, the virtual work of the aerodynamic forces can be written as

$$\delta \bar{W} = \int_0^L \left[ L' \delta w + (MAC' + L' \left( \frac{1}{2} + a \right) b \delta \theta \right] dy \quad (9)$$

The displacement  $w$  and the rotation  $\theta$  are assumed to be a superposition of the mode shapes, with a modal truncation considered for the analysis :

$$\begin{aligned} w(y, t) &= \sum_{i=1}^{N_w} \eta_i(t) \Psi_i(y) \\ \theta(y, t) &= \sum_{i=1}^{N_\theta} \phi_i(t) \Theta_i(y) \end{aligned} \quad (10)$$

where  $\Psi_i$  and  $\Theta_i$  are respectively the  $i$ -th bending and torsion mode shapes. The derivation of the bending and torsion mode shapes is provided in the appendix. The bending mode shape  $\Psi_i$  is defined as :

$$\Psi_i(y) = [\cosh(\alpha_i y) - \cos(\alpha_i y)] - \beta_i [\sinh(\alpha y) - \sin(\alpha y)]$$

and the torsion mode shape  $\Theta_i$  is defined as :

$$\Theta_i(y) = \sqrt{2} \sin(\gamma_i y)$$

For the definitions of  $\alpha_i$ ,  $\beta_i$ , and  $\gamma_i$ , refer to the appendix. Substituting the expressions for  $w$  and  $\theta$  into the definitions of the potential energy results in:

$$PE = \frac{1}{2} \int_0^L \left[ EI \left( \sum_{i=1}^{N_w} \eta_i(t) \Psi_i''(y) \right)^2 + GJ \left( \sum_{i=1}^{N_\theta} \phi_i(t) \Theta_i'(y) \right)^2 \right] dy$$

Since bending modes are orthogonal to each other and torsion modes are also orthogonal to each other, this equation simplifies into :

$$PE = \frac{1}{2} \sum_{i=1}^{N_w} \eta_i^2(t) \int_0^L EI (\Psi_i'')^2 dy + \frac{1}{2} \sum_{i=1}^{N_\theta} \phi_i^2(t) \int_0^L GJ (\Theta_i')^2 dy$$

A careful computation of the integrals yields :

$$PE = \frac{1}{2} \left[ \frac{EI}{L^3} \sum_{i=1}^{N_w} (\alpha_i L)^4 \eta_i^2(t) + \frac{GJ}{L} \sum_{i=1}^{N_\theta} (\gamma_i L)^2 \phi_i^2(t) \right]$$

Similarly for the kinetic energy, we obtain :

$$\begin{aligned} KE &= \frac{1}{2} \int_0^L \left( m \left( \sum_{i=1}^{N_w} \dot{\eta}_i \Psi_i \right)^2 + mb^2 r^2 \left( \sum_{i=1}^{N_\theta} \dot{\phi}_i \Theta_i \right)^2 \right. \\ &\quad \left. - 2mbx_\theta \sum_{i=1}^{N_w} \sum_{j=1}^{N_\theta} \dot{\eta}_i \dot{\phi}_j \Psi_i \Theta_j \right) dy \end{aligned}$$

Using the orthogonality of the bending and torsion modes, this equation simplifies to:

$$\begin{aligned} KE &= \frac{1}{2} \left( m \sum_{i=1}^{N_w} \dot{\eta}_i^2 \int_0^L \Psi_i^2 dy + mb^2 r^2 \sum_{i=1}^{N_\theta} \dot{\phi}_i^2 \int_0^L \Theta_i^2 dy \right. \\ &\quad \left. - 2mbx_\theta \sum_{i=1}^{N_w} \sum_{j=1}^{N_\theta} \dot{\eta}_i \dot{\phi}_j \int_0^L \Psi_i \Theta_j dy \right) \end{aligned}$$

A careful evaluation of the integrals yields to :

$$KE = \frac{mL}{2} \left( \sum_{i=1}^{N_w} \dot{\eta}_i^2 + b^2 r^2 \sum_{j=1}^{N_\theta} \dot{\phi}_j^2 - 2bx_\theta \sum_{i=1}^{N_w} \sum_{j=1}^{N_\theta} \dot{\eta}_i \dot{\phi}_j A_{i,j} \right)$$

where :  $A_{i,j} = \frac{1}{L} \int_0^L \Psi_i \Theta_j dy$  For the virtual-work expression, we obtain :

$$\delta \bar{W} = \sum_{i=1}^{N_w} \delta \eta_i \left( \int_0^L \Psi_i L' dy \right) + \sum_{i=1}^{N_\theta} \delta \phi_i \left( \int_0^L \Theta_i M'_{e,a} dy \right)$$

With the expressions for kinetic energy (KE), potential energy (PE), and the generalized forces, we have all the necessary components to apply Lagrange's equations and derive the equations of motion for the system. For the generalized coordinates  $\eta_i$ , we have :

$$mL \left( \ddot{\eta}_i - 2bx_\theta \sum_{j=1}^{N_\theta} A_{i,j} \ddot{\phi}_j \right) + \overline{EI}(\alpha_i L)^4 \eta_i = \int_0^L \Psi_i L' dy$$

For the generalized coordinates  $\phi_i$ , we have :

$$mL \left( b^2 r^2 \ddot{\phi}_i - 2bx_\theta \sum_{i=1}^{N_w} A_{i,j} \ddot{\eta}_i \right) + \frac{\overline{GJ}}{L} (\gamma_i L)^2 \phi_i = \int_0^L \Theta_i M'_{e,a} dy$$

This system of equation can be written in a matrix form :

$$mL \begin{pmatrix} \mathbf{I}_{N_w} & -2bx_\theta \mathbf{A} \\ -2bx_\theta \mathbf{A}^T & b^2 r^2 \mathbf{I}_{N_\theta} \end{pmatrix} \begin{pmatrix} \ddot{\eta} \\ \ddot{\phi} \end{pmatrix} + \begin{pmatrix} \frac{\overline{EI}}{L^3} [\alpha \mathbf{L}]^4 & \mathbf{0}_{N_w \times N_\theta} \\ \mathbf{0}_{N_\theta \times N_w} & \frac{\overline{GJ}}{L} [\gamma \mathbf{L}]^2 \end{pmatrix} \begin{pmatrix} \ddot{\eta} \\ \ddot{\phi} \end{pmatrix} = \begin{pmatrix} \int_0^L \ddot{\Psi} L' dy \\ \int_0^L \ddot{\Theta} M'_{e,a} dy \end{pmatrix}$$

Where:  $\mathbf{I}_{N_w}$  is the identity matrix of size  $N_w$ ,  $\mathbf{I}_{N_\theta}$  is the identity matrix of size  $N_\theta$ ,  $[\alpha \mathbf{L}]^4$  is the diagonal matrix with entries  $(\alpha_i L^4)$ , and  $[\gamma \mathbf{L}]^2$  is the diagonal matrix with entries  $(\gamma_i L^2)$ . The expression for the right-hand side (generalized forces) is derived using Theodorsen's theory :

$$L' = 2\pi\rho_\infty U b C(k) \left[ U\theta - \frac{\partial w}{\partial t} + b \left( \frac{1}{2} - a \right) \frac{\partial \theta}{\partial t} \right] + \pi\rho_\infty b^2 \left[ U \frac{\partial \theta}{\partial t} - \frac{\partial^2 w}{\partial t^2} - ba \frac{\partial^2 \theta}{\partial t^2} \right]$$

and :

$$M'_{e,a} = -\pi\rho_\infty b^3 \left[ U \frac{\partial \theta}{\partial t} - \frac{1}{2} \frac{\partial^2 w}{\partial t^2} + b \left( \frac{1}{8} - \frac{a}{2} \right) \frac{\partial^2 \theta}{\partial t^2} \right] + L' \left( \frac{1}{2} + a \right) b$$

Using the assumed expressions for  $w$  and  $\theta$ , we obtain after calculations :

$$\begin{pmatrix} \int_0^L \ddot{\Psi} L' dy \\ \int_0^L \ddot{\Theta} M'_{e,a} dy \end{pmatrix} = -\pi\rho_\infty b^2 L \begin{pmatrix} \mathbf{I}_{N_w} & ba\mathbf{A} \\ ba\mathbf{A}^T & (b^2 a^2 + \frac{1}{8}) \mathbf{I}_{N_\theta} \end{pmatrix} \begin{pmatrix} \ddot{\eta} \\ \ddot{\phi} \end{pmatrix} - \pi\rho b U L \begin{pmatrix} 2C(k)\mathbf{I} & -b[1 + 2[\frac{1}{2} - a]C(k)]\mathbf{A} \\ 2b(\frac{1}{2} + a)C(k)\mathbf{A}^T & b^2(\frac{1}{2} - a)[1 - 2[\frac{1}{2} + a]C(k)]\mathbf{I} \end{pmatrix} \begin{pmatrix} \ddot{\eta} \\ \ddot{\phi} \end{pmatrix} - \pi\rho_\infty b U^2 L \begin{pmatrix} \mathbf{0}_{N_w} & -2C(k)\mathbf{A} \\ \mathbf{0}_{N_\theta} & -b(1 + 2a)C(k)\mathbf{I}_{N_\theta} \end{pmatrix} \begin{pmatrix} \ddot{\eta} \\ \ddot{\phi} \end{pmatrix}$$

To apply the  $p - k$  method, we use the following expressions: for the structural terms,

$$\ddot{\eta} = \ddot{\eta} e^{\frac{pU}{b}t}, \quad \ddot{\phi} = \ddot{\phi} e^{\frac{pU}{b}t},$$

and for the aerodynamic terms,

$$\ddot{\eta} = \ddot{\eta} e^{i\frac{kU}{b}t}, \quad \ddot{\phi} = \ddot{\phi} e^{i\frac{kU}{b}t}.$$

Thus, we have :

$$\begin{pmatrix} p^2 \frac{mLU^2}{b^2} \mathbf{I}_{N_w} + \frac{\overline{EI}}{L^3} [\alpha \mathbf{L}]^4 & -2p^2 x_\theta \frac{mLU^2}{b} \mathbf{A} \\ -2p^2 x_\theta \frac{mLU^2}{b} \mathbf{A}^T & r^2 p^2 \frac{mLU^2}{b} \mathbf{I}_{N_\theta} + \frac{\overline{GJ}}{L} [\gamma \mathbf{L}]^2 \end{pmatrix} \begin{pmatrix} \ddot{\eta} \\ \ddot{\phi} \end{pmatrix} e^{\frac{pU}{b}t} = \begin{pmatrix} \frac{k^2 U^2}{b^2} \pi\rho_\infty L \begin{pmatrix} \mathbf{I}_{N_w} & ba\mathbf{A} \\ ba\mathbf{A}^T & (b^2 a^2 + \frac{1}{8}) \mathbf{I}_{N_\theta} \end{pmatrix} \\ -i\pi\rho U^2 L k \begin{pmatrix} 2C(k)\mathbf{I} & -b[1 + 2[\frac{1}{2} - a]C(k)]\mathbf{A} \\ 2b(\frac{1}{2} + a)C(k)\mathbf{A}^T & b^2(\frac{1}{2} - a)[1 - 2[\frac{1}{2} + a]C(k)]\mathbf{I} \end{pmatrix} \\ -\pi\rho_\infty b U^2 L \begin{pmatrix} \mathbf{0}_{N_w} & -2C(k)\mathbf{A} \\ \mathbf{0}_{N_\theta} & -b(1 + 2a)C(k)\mathbf{I}_{N_\theta} \end{pmatrix} \end{pmatrix} \begin{pmatrix} \ddot{\eta} \\ \ddot{\phi} \end{pmatrix} e^{i\frac{kU}{b}t}$$

At the flutter boundary, we have:  $p = ik$ , so the equations simplify to:

$$\begin{pmatrix} p^2 \frac{mLU^2}{b^2} \mathbf{I}_{N_w} + \frac{\overline{EI}}{L^3} [\alpha \mathbf{L}]^4 & -2p^2 x_\theta \frac{mLU^2}{b} \mathbf{A} \\ -2p^2 x_\theta \frac{mLU^2}{b} \mathbf{A}^T & r^2 p^2 \frac{mLU^2}{b} \mathbf{I}_{N_\theta} + \frac{\overline{GJ}}{L} [\gamma \mathbf{L}]^2 \end{pmatrix} - \begin{pmatrix} \frac{k^2 U^2}{b^2} \pi\rho_\infty L \begin{pmatrix} \mathbf{I}_{N_w} & ba\mathbf{A} \\ ba\mathbf{A}^T & (b^2 a^2 + \frac{1}{8}) \mathbf{I}_{N_\theta} \end{pmatrix} \\ +i\pi\rho U^2 L k \begin{pmatrix} 2C(k)\mathbf{I} & -b[1 + 2[\frac{1}{2} - a]C(k)]\mathbf{A} \\ 2b(\frac{1}{2} + a)C(k)\mathbf{A}^T & b^2(\frac{1}{2} - a)[1 - 2[\frac{1}{2} + a]C(k)]\mathbf{I} \end{pmatrix} \\ +\pi\rho_\infty b U^2 L \begin{pmatrix} \mathbf{0}_{N_w} & -2C(k)\mathbf{A} \\ \mathbf{0}_{N_\theta} & -b(1 + 2a)C(k)\mathbf{I}_{N_\theta} \end{pmatrix} \end{pmatrix} \begin{pmatrix} \ddot{\eta} \\ \ddot{\phi} \end{pmatrix} = \vec{0}$$

To prevent non-trivial solutions, the determinant of this matrix must be set to zero. This determinant will yield a polynomial in  $p$  of degree  $2(N_w + N_\theta)$ . Consequently, the approach to solving this problem follows a procedure similar to that in Algorithm 1, except that we now have  $2(N_w + N_\theta)$  roots to converge at each velocity  $U$ . Analysis is performed for the initial design in the empty wing configuration at an altitude of  $h = 1.5km$ . The analysis considered only the first bending mode and the first pitching mode of a uniform flexible wing to compare with the results presented in figures 9 and 10. Results are presented in figures 21 and 22. The results are comparable to those obtained using the traditional method, although the flutter velocity is slightly lower than that predicted by the traditional approach. Due to time constraints, we could not include additional pitching and bending modes in the analysis. Nevertheless, the results are promising, and further analyses are recommended.

## 8. Summary and conclusions

In conclusion, the study of aeroelasticity for the initial aircraft design revealed critical deficiencies in both divergence speed and flutter speed, which failed to meet or barely comply with the regulatory requirements. A comprehensive modification to the rear wing structure was proposed, leveraging high-performance materials to shift the center of mass forward. This adjustment successfully brought the design into compliance with the required regulations, ensuring safety and stability across the operational flight envelope.



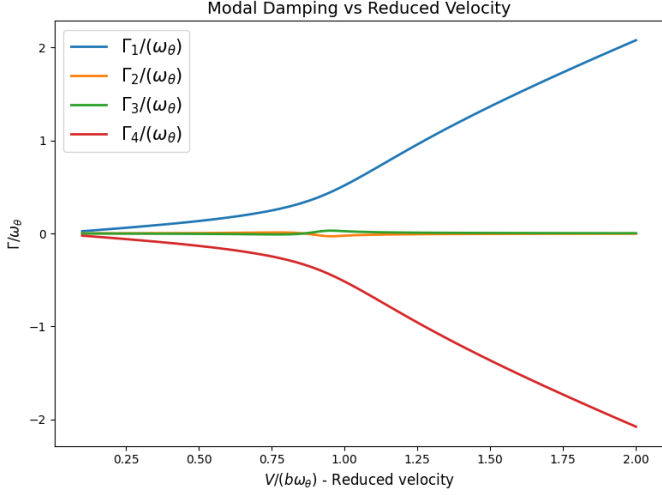


Figure 21: Evolution of modal damping with respect to the reduced velocity. p-k method with assumed mode shapes.

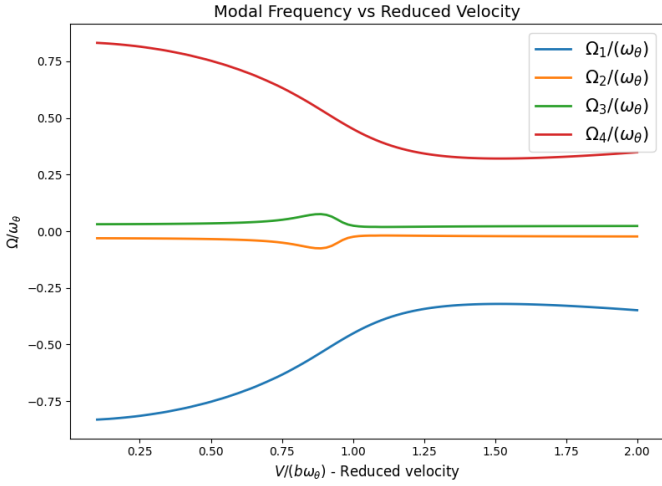


Figure 22: Evolution of modal frequency with respect to the reduced velocity. p-k method with assumed mode shapes.

Additionally, the study extended the analysis to evaluate the aeroelastic behavior of an all-electric variant of the aircraft. Despite the significant mass redistribution introduced by battery storage, the proposed designs demonstrated regulatory compliance under specific operational constraints. This analysis provides a foundational framework for exploring electric propulsion's feasibility in general aviation, highlighting both opportunities and challenges related to environmental impact, operational endurance, and design trade-offs.

A novel contribution of this study was the application of a new method utilizing modal shapes of vibration in the p-k method framework. This approach yielded consistent results with traditional techniques while offering a pathway to more detailed aeroelastic characterization. The method holds potential for further refinement and broader application in similar aeroelastic studies.

While the approaches and findings outlined in this paper are appropriate for the pre-design phase, it is crucial to acknowl-

edge their limitations. Future work should incorporate higher fidelity models, including the effects of three-dimensional aerodynamics and non-linear structural dynamics, to provide a more comprehensive evaluation of the aeroelastic performance. Experimental validation through wind tunnel testing or flight tests will also be indispensable as the design matures.

Lastly, this study underscores the importance of iterative design in addressing aeroelastic challenges, emphasizing the balance between regulatory compliance, operational performance, and environmental considerations. The findings serve as a stepping stone for further innovation in the development of both conventional and electric aircraft designs, paving the way for safer and more sustainable aviation solutions.

## Statement of contributions

Corentin Latimier focused on the development and validation of the p-k method, as well as the analysis of the flight envelope and flutter for the standard aircraft configuration. Manuel Sandoval concentrated on divergence analysis for the aircraft, and the flutter analysis and design constraints for the electric version.

Both collaborated on writing the report, including the abstract, introduction, theoretical framework, economic and environmental impact assessments, and conclusions.

For the bonus part, Manuel Sandoval focused on using MSC Nastran to numerically simulate the configuration, while Corentin Latimier focused on implementing the Assumed Modes method within the  $p - k$  framework, which was presented given its relevance to the project.

## Appendix A. Bending modes derivation

We analyze a uniform beam aligned along the  $y$ -axis, undergoing bending in the  $z$ -direction. The potential energy density is described by:

$$\overline{PE}(y) = \frac{\overline{EI}}{2} \left( \frac{\partial^2 w}{\partial y^2} \right)^2 = \frac{\overline{EI}}{2} (w'')^2,$$

while the kinetic energy density is:

$$\overline{KE}(y) = \frac{\rho A}{2} \dot{w}^2.$$

This formulation assumes that rotational effects in the beam sections are negligible. Using Hamilton's principle, the governing equation is:

$$\delta \int_{t_1}^{t_2} \int_0^L [\overline{KE} - \overline{PE}] dy dt = 0,$$

with the boundary condition  $\delta w(t_1) = \delta w(t_2) = 0$ .

By applying the variation operator  $\delta$  to the integrals, the expression simplifies to:

$$\int_{t_1}^{t_2} \int_0^L \left[ \frac{\partial \overline{KE}}{\partial \dot{w}} \delta \dot{w} - \frac{\partial \overline{PE}}{\partial w''} \delta w'' \right] dy dt = 0.$$



We have :

$$\int_{t_1}^{t_2} \frac{\partial \overline{KE}}{\partial \dot{w}} \delta \dot{w} dt = \left[ \frac{\partial \overline{KE}}{\partial \dot{w}} \delta w \right]_{t_1}^{t_2} - \int_{t_1}^{t_2} \frac{d}{dt} \left[ \frac{\partial \overline{KE}}{\partial \dot{w}} \right] \delta w dt$$

and using two integration by parts :

$$\begin{aligned} \int_0^L \frac{\partial \overline{PE}}{\partial w'''} \delta w''' dy &= \left[ \frac{\partial \overline{PE}}{\partial w''} \delta w' \right]_0^L - \left[ \frac{\partial}{\partial y} \left( \frac{\partial \overline{PE}}{\partial w''} \right) \delta w \right]_0^L \\ &+ \int_0^L \frac{\partial^2}{\partial^2 y} \left[ \frac{\partial \overline{PE}}{\partial w''} \right] \delta w dy \end{aligned}$$

Therefore, using the fact that  $\delta w(t_1) = \delta w(t_2)$ , we arrive at :

$$\begin{aligned} - \int_{t_1}^{t_2} \int_0^L \left( \frac{d}{dt} \left[ \frac{\partial \overline{KE}}{\partial \dot{w}} \right] + \frac{\partial^2}{\partial^2 y} \left[ \frac{\partial \overline{PE}}{\partial w''} \right] \right) \delta w dy dt - \left[ \frac{\partial \overline{PE}}{\partial w''} \delta w' \right]_0^L \\ - \left[ \frac{\partial}{\partial y} \left( \frac{\partial \overline{PE}}{\partial w''} \right) \delta w \right]_0^L = 0 \quad \forall \delta w \end{aligned}$$

Therefore, since this equation must hold for all variations  $\delta w$ , the term inside the integral must be zero, leading to the equation governing the vibration of a beam in bending. Additionally, the terms in the brackets must also vanish, resulting in :

$$\begin{cases} \rho A \frac{\partial^2 w}{\partial t^2} + \overline{EI} \frac{\partial^4 w}{\partial y^4} = 0 \\ w(0) = 0, \quad \frac{\partial w}{\partial y}(0) = 0 \\ \frac{\partial^3 w}{\partial y^3}(L) = 0, \quad \frac{\partial^4 w}{\partial y^4}(L) = 0 \end{cases}$$

Assuming that the solution for  $w$  can be expressed as:

$$w(y, t) = \Psi(y)T(t),$$

substituting this into the governing equations results in:

$$\begin{aligned} \rho A \ddot{T} \Psi(y) + \overline{EI} T(t) \Psi^{(4)}(y) &= 0, \\ \iff \frac{\Psi^{(4)}}{\Psi} &= -\frac{\rho A}{\overline{EI}} \frac{\ddot{T}}{T}. \end{aligned}$$

The left-hand side depends only on  $y$ , while the right-hand side depends only on  $t$ . Therefore, both sides must be equal to a constant  $\alpha^4$ , leading to the following equation:

$$\frac{\Psi^{(4)}}{\Psi} = -\frac{\rho A}{\overline{EI}} \frac{\ddot{T}}{T} = \alpha^4$$

The equation for  $\Psi(y)$  is a well-known fourth-order differential equation, and its solution is given by:

$$\Psi(y) = A \cos(\alpha y) + B \cosh(\alpha y) + C \sin(\alpha y) + D \sinh(\alpha y)$$

and for  $T$ , we have :

$$T(t) = E \cos(\omega t) + F \sin(\omega t)$$

with  $\omega = \alpha^2 \sqrt{\frac{\overline{EI}}{\rho A}}$ . To determine the mode shapes, we must apply the boundary conditions for a clamped-free beam. At  $y = 0$ , we have :

$$\begin{aligned} \Psi(0) = 0 &\iff A + B = 0 \\ \Psi'(0) = 0 &\iff C + D = 0 \end{aligned}$$

Therefore,

$$\Psi(y) = A [\cos(\alpha y) - \cosh(\alpha y)] + C [\sin(\alpha y) - \sinh(\alpha y)]$$

Using the boundary conditions at  $y = L$ , we must have :

$$\begin{aligned} \Psi''(L) = 0 &\iff A [-\cos(\alpha L) - \cosh(\alpha L)] \\ &+ C [-\sin(\alpha L) - \sinh(\alpha L)] = 0 \end{aligned}$$

and

$$\begin{aligned} \Psi'''(L) = 0 &\iff A [\sin(\alpha L) - \sinh(\alpha L)] \\ &+ C [-\cos(\alpha L) - \cosh(\alpha L)] = 0 \end{aligned}$$

Therefore, we have the system of equations

$$\begin{pmatrix} -\cos(\alpha L) - \cosh(\alpha L) & -\sin(\alpha L) - \sinh(\alpha L) \\ \sin(\alpha L) - \sinh(\alpha L) & -\cos(\alpha L) - \cosh(\alpha L) \end{pmatrix} \begin{pmatrix} A \\ C \end{pmatrix} = \begin{pmatrix} 0 \\ 0 \end{pmatrix}$$

The determinant of the coefficient matrix must be zero for a non-trivial solution, so we compute the determinant:

$$\begin{aligned} \cos^2(\alpha L) + 2 \cos(\alpha L) \cosh(\alpha L) + \cosh^2(\alpha L) + \sin^2(\alpha L) - \sinh^2(\alpha L) &= 0 \\ \iff 2 + 2 \cos(\alpha L) \cosh(\alpha L) &= 0 \end{aligned}$$

$$\iff -\cos(\alpha L) = \frac{1}{\cosh(\alpha L)}$$

This equation admits multiple solutions denoted as  $\alpha_i L$ . For a given solution, the corresponding pulsation can be found :

$$\omega_i = \alpha_i^2 \sqrt{\frac{\overline{EI}}{\rho A}}$$

To find the constant  $A$  and  $B$ , we can consider the second equation of the matrix system :

$$A_i [\sin(\alpha_i L) - \sinh(\alpha_i L)] = C_i [\cos(\alpha_i L) + \cosh(\alpha_i L)]$$

Using  $A_i = -1$ , we have :

$$C_i = \frac{-\sin(\alpha_i L) + \sinh(\alpha_i L)}{\cos(\alpha_i L) + \cosh(\alpha_i L)}$$

We define  $\beta_i = C_i$  and we obtain :

$$\Psi_i(y) = [\cosh(\alpha_i y) - \cos(\alpha_i y)] - \beta_i [\sinh(\alpha y) - \sin(\alpha y)]$$

## Appendix B. Torsion modes derivation

We consider a uniform beam subjected to torsion along the  $y$ -axis. Its density of potential energy due to deformation is expressed as:

$$\overline{PE} = \frac{\overline{GJ}}{2} \left[ \frac{\partial \theta}{\partial y} \right]^2$$

The density of kinetic energy can be expressed as :

$$\overline{KE} = \frac{\overline{\rho I}}{2} \left[ \frac{\partial \theta}{\partial t} \right]^2$$

Using Hamilton's principle, the governing equation is :

$$\delta \int_{t_1}^{t_2} \int_0^L \overline{KE} - \overline{PE} dy dt = 0$$

with the boundary condition :  $\delta\theta(t_1) = \delta\theta(t_2) = 0$ . This equation can be expanded as :

$$\int_{t_1}^{t_2} \int_0^L \frac{\partial \overline{KE}}{\partial \dot{\theta}} \delta \dot{\theta} - \frac{\partial \overline{PE}}{\partial \theta'} \delta \theta' dy dt = 0$$

We have :

$$\int_{t_1}^{t_2} \frac{\partial \overline{KE}}{\partial \dot{\theta}} \delta \dot{\theta} dt = \left[ \frac{\partial \overline{KE}}{\partial \dot{\theta}} \delta \theta \right]_0^L - \int_{t_1}^{t_2} \frac{\partial}{\partial t} \left[ \frac{\partial \overline{KE}}{\partial \dot{\theta}} \right] \delta \theta dt$$

and :

$$\int_0^L \frac{\partial \overline{PE}}{\partial \theta'} \delta \theta' dy = \left[ \frac{\partial \overline{PE}}{\partial \theta'} \delta \theta \right]_0^L - \int_0^L \frac{\partial}{\partial y} \left[ \frac{\partial \overline{PE}}{\partial \theta'} \right] \delta \theta dy$$

Therefore, we obtain :

$$\begin{aligned} \int_{t_1}^{t_2} \int_0^L \left( -\frac{d}{dt} \left[ \frac{\partial \overline{KE}}{\partial \dot{\theta}} \right] + \frac{\partial}{\partial y} \left[ \frac{\partial \overline{PE}}{\partial \theta'} \right] \right) \delta \theta dy dt \\ - \int_{t_1}^{t_2} \left[ \frac{\partial \overline{PE}}{\partial \theta'} \delta \theta \right]_0^L dt = 0 \end{aligned}$$

Since this equation must hold for all variations  $\delta\theta$ , the term inside the integral must be zero, leading to the equation governing the vibration of a beam in torsion. Additionally, the terms in the brackets must also vanish, resulting in :

$$\begin{cases} \rho I \frac{\partial^2 \theta}{\partial t^2} = \overline{GJ} \frac{\partial^2 \theta}{\partial y^2}, \\ \theta(0) = 0, \quad \frac{\partial \theta}{\partial y}(L) = 0. \end{cases}$$

Assuming that the solution can be expressed as :

$$\theta(y, t) = \Theta(y)T(t)$$

and inserting this form in the governing equation yields :

$$\begin{aligned} \rho I \Theta T''(t) &= \overline{GJ} T \Theta''(y) \\ \Leftrightarrow \frac{\Theta''(y)}{\Theta} &= \frac{\rho I}{\overline{GJ}} \frac{T''(t)}{T} \end{aligned}$$

The left-hand side depends only on  $y$ , while the right-hand side depends only on  $t$ . Therefore, both sides must be equal to a constant  $-\gamma^2$ , leading to the following equation:

$$\frac{\Theta''(y)}{\Theta} = \frac{\rho I}{\overline{GJ}} \frac{T''(t)}{T} = -\gamma^2$$

The solutions are well-known and can be written as :

$$\Theta(y) = A \cos(\gamma y) + B \sin(\gamma y)$$

$$T(t) = C \cos(\omega t) + D \sin(\omega t)$$

$$\text{with } \omega = \gamma \sqrt{\frac{\overline{GJ}}{\rho I}}$$

To find the mode shapes, we use the boundary conditions :

$$\theta(0) = 0 \iff A = 0$$

and

$$\frac{\partial \theta}{\partial y}(L) = 0 \iff B \gamma \cos(\gamma L) = 0$$

To avoid a non trivial solution, we must have :

$$\gamma_i = \frac{(2i-1)\pi}{2L}$$

We arbitrarily set  $B = \sqrt{2}$ , which leads to the mode shapes being defined as:

$$\Theta_i(y) = \sqrt{2} \sin(\gamma_i y)$$

## Appendix C. P-K Method implementation - Codes

The codes developed in Python for the aeroelastic analysis, namely implementation of the p-k method and its validation, are provided as attachments to the paper.

## References

- [1] F. Register, The federal register (2005).
- [2] E. Jonsson, C. Riso, C. A. Lupp, C. E. Cesnik, J. R. Martins, B. I. Epureanu, Flutter and post-flutter constraints in aircraft design optimization, Progress in Aerospace Sciences 109 (2019) 100537. doi:https://doi.org/10.1016/j.paerosci.2019.04.001.
- [3] S. Gudmundsson, Chapter 9 - the anatomy of the wing, in: S. Gudmundsson (Ed.), General Aviation Aircraft Design, Butterworth-Heinemann, Boston, 2014, pp. 299–399. doi:https://doi.org/10.1016/B978-0-12-397308-5.00009-X.
- [4] J. Anderson, Fundamentals of Aerodynamics, McGraw-Hill Education, 2010.
- [5] H. J. HASSIG, An approximate true damping solution of the flutter equation by determinant iteration., Journal of Aircraft 8 (11) (1971) 885–889. doi:10.2514/3.44311.
- [6] R. H. Scanlan, R. A. Rosenbaum, Introduction to the study of aircraft vibration and flutter, The Journal of the Royal Aeronautical Society 56 (1952) 59 – 60.
- [7] T. Theodorsen, General theory of aerodynamic instability and the mechanism of flutter, 1934. URL <https://api.semanticscholar.org/CorpusID:118032051>
- [8] D. Hodges, G. Pierce, Introduction to Structural Dynamics and Aeroelasticity, 2011. doi:10.1017/CBO9780511809170.
- [9] ISA, Standard atmosphere (1975).
- [10] Xu, Suoao, Nanostructured materials for energy storage in future electric aircraft, E3S Web of Conf. 553 (2024) 02021. doi:10.1051/e3sconf/202455302021.
- [11] J. Christy, Engines for Homebuilt Aircraft & Ultralights, Tab Books, 1983.
- [12] M. Idres, Assessment of the range of an electric aircraft, Journal of Advanced Research in Applied Sciences and Engineering Technology 50 (2) (2025) 155–170.
- [13] HydroQuebec, Comparison of electricity prices in major north american cities, <https://www.hydroquebec.com/data/documents-donnees/pdf/comparis> [Accessed 15-12-2024] (2023).
- [14] JetFuel, Avgas price in canada, <https://jet-a1-fuel.com/avgas/canada>, [Accessed 15-12-2024].
- [15] C. A. A. M. Consortium, Aam and environment sustainability: The environmental and social impacts of lithium-ion batteries, <https://canadianaam.com/2022/09/22/aam-and-environment-sustainability> [Accessed 15-12-2024] (2022).